RSC Advances

PAPER

View Article Online
View Journal | View Issue

Cite this: *RSC Adv.*, 2022, **12**, 25578

Structural elucidation of hexavalent Cr adsorbed on surfaces and bulks of Fe_3O_4 and α-FeOOH†

Nichapha Senamart,[a] Krittanun Deekamwong,[b] Jatuporn Wittayakun,[b] Sanchai Prayoonpokarach,[b] Narong Chanlek,[c] Yingyot Poo-arporn,[c] Suttipong Wannapaiboon,[c] Pinit Kidkhunthod[c] and Sirinuch Loiha*[a]

Magnetite (Fe_3O_4) and goethite (α-FeOOH) were synthesized *via* a hydrothermal approach and utilized as adsorbents for Cr^{6+} removal in an aqueous medium. The typical crystal structures of the synthesized Fe_3O_4 and α-FeOOH were confirmed by XRD and TEM. Fe_3O_4 in a spherical shape with a surface area of 32 m^2 g^{-1} was established. While α-FeOOH had a rod-like form with a larger surface area of 84 m^2 g^{-1}. Cr^{6+} removal in an aqueous solution was studied in various conditions to evaluate thermodynamic and kinetic parameters. The adsorption isotherms on both adsorbents fit the Langmuir model indicating monolayer adsorption. Fe_3O_4 showed a better adsorption ability than α-FeOOH even though it had a lower surface area. XAS and XPS analysis strongly evidenced the production of stable Cr^{3+} species of $Fe_{(1-x)}Cr_xOOH$ and $Fe_{(3-x)}Cr_xO_4$ by Cr^{6+} reduction and migration processes into the bulk structure. Thus, the existence of stable Cr-species in Fe_3O_4 structure strongly affected Cr-adsorption ability rather than the surface area of the adsorbent. However, the precipitated Cr_2O_3 and $HCrO_4^-$ molecules electrostatically adsorbed on the outer surface of α-FeOOH without bulk transformation. The presence of physisorbed FeO–$HCrO_4$ species on α-FeOOH led to low reducibility and adsorption capability of Cr^{6+}.

Received 16th June 2022
Accepted 30th August 2022

DOI: 10.1039/d2ra03676b

rsc.li/rsc-advances

Introduction

Hexavalent Cr^{6+} ions are toxic contaminants because of their mutagenicity, carcinogenicity, and teratogenicity.[1–5] Toxic Cr^{6+} species generally exist in negatively charged forms, such as the ions of hydrogen chromate ($HCrO_4^-$), chromate (CrO_4^{2-}), and dichromate ($Cr_2O_7^{2-}$), depending on solution pH and concentration.[6,7] However, no conclusive spectroscopic proof of structural changes in adsorbents and adsorbates is available.[8,9] X-Ray absorption spectroscopy (XAS) is a powerful tool for the element-specific characterization of local structure and chemistry. The electronic and local structures or geometry of chromium species in water will be explored. Understanding the stabilized Cr-species on the adsorbents is beneficial to the development of new materials from the waste treatment process. Wei *et al.*[10] illustrated the determination of Cr-contamination in kitchen wastewater by XAS. The Cr-species distribution in the solution was estimated. Likewise, Meena and Arai[11] could explore the Cr^{3+}/Cr^{6+} ratio and Cr-structures on Fe_3O_4 through the Cr-adsorption process from groundwater by using X-ray absorption near edge structure (XANES) and extended X-ray absorption fine structure (EXAFS) analysis.

Different techniques, such as chemical precipitation, adsorption, photocatalysis, and reduction using cationic materials, are available for the removal of Cr^{6+} from wastewater.[7,12–16] Utilization of natural-cationic materials, such as activated carbon, chitosan, chelate resins, and natural zeolites for Cr^{6+} adsorption has been widely investigated due to their low cost, feasibility, handling simplicity, and flexibility.[17–20] However, the removal of the adsorbed Cr^{6+} species by those adsorbents still needs a further reduction process to complete the Cr disposal.

Chemical reduction using environment-friendly materials, such as iron oxides, is an interesting alternative method for Cr^{6+} removal from wastewater.[21,22] Iron (oxy) hydroxide of goethite (α-FeOOH) containing Fe^{3+} is a potential Cr^{6+} adsorbent due to its high surface area and thermal stability.[7,23] Moreover, octahedral sites of Fe^{3+} in orthorhombic α-FeOOH structure play a significant role in Cr^{6+} adsorption. In addition, the presence of a small amount of Fe^{2+} species on the α-FeOOH surface provides a great reduction potential for Cr^{6+} ions.[24] However, a drawback of polymorphs of the synthetic α-FeOOH formed in acidic conditions leads to an additional protonation, resulting in structure destabilization.[7,25,26] Hence, the preparation of a stable α-FeOOH structure with uniform crystalline needs to be investigated. Additionally, the metal oxide of Fe_3O_4 (magnetite) or ferrous-ferric iron oxide nature is interesting for Cr^{6+} removal

[a]*Center for Innovation in Chemistry (PERCH-CIC), Materials Chemistry Research Center, Department of Chemistry, Faculty of Science, Khon Kaen University, Khon Kaen 40002, Thailand. E-mail: sirilo@kku.ac.th*

[b]*School of Chemistry, Institute of Science, Suranaree University of Technology, Nakhon Ratchasima, 30000, Thailand*

[c]*Synchrotron Light Research Institute, Nakhon Ratchasima 30000, Thailand*

† Electronic supplementary information (ESI) available. See https://doi.org/10.1039/d2ra03676b

because it has a suitable redox potential for Cr^{6+} reduction and excellent magnetic properties.[27,28] It is widely known that Fe^{2+} in magnetite can reduce Cr^{6+} to Cr^{3+} creating Cr^{3+}-hydroxide or mixed substances *via* an adsorption and reduction process, namely reductive precipitation.[29,30] This adsorption behavior on the Fe_3O_4 surface was explored and Cr^{3+} and Fe^{3+}-(oxy)hydroxides were passivated on the adsorbent surface.[30] The adsorption ability and structural stability of Fe_3O_4 are strongly affected by solution pH and the homogeneity of iron oxide particles. The effect of the passivation layer on bulk structure deserves our study. In addition, the relationship between adsorption ability and phase stability in bulk-iron oxides needs to be investigated. Understanding the stable Cr-forms on the ion-oxides is promising for catalyst applications.[31]

In the present study, iron oxides of Fe_3O_4 and α-FeOOH were synthesized by the hydrothermal method and used as Cr^{6+} adsorbents. The crystalline structure, morphology, and surface area of the bare and adsorbed materials were characterized. The Cr-adsorption ability and behavior were explored. The adsorbent surfaces and bulk structures were elucidated by XPS and XAS.

Experimental

Materials and methods

Materials. The chemicals including iron(III) nitrate nonahydrate ($Fe(NO_3)_3 \cdot 9H_2O$, 98%, Merck), iron(III) chloride ($FeCl_3$, 98%, ACROS), potassium dichromate ($K_2Cr_2O_7$, 99.9%, LOBA), sodium acetate (NaOAc, 99.5%, LOBA), potassium hydroxide pallets (KOH, 85%, LOBA), hydrochloric acid (HCl, 37%, QRëC™), ethylene glycol (EG, AR grade, QRëC™) and 1, 5-diphenylcabazone (50% diphenylcabazid, ACS grade, Merck) were used in this work.

Methods. The crystal structures of α-FeOOH and Fe_3O_4 were revealed by powder X-ray diffraction (XRD; PANalytical, EMPYREAN). The XRD patterns were indexed by Match! Software using the Crystallography Open Database (COD), which was available at Beamline 1.1 W (Multiple X-ray Techniques), Synchrotron Light Research Institute, Thailand, SLRI. The unit cell parameters are refined by using FullProf Software. Morphologies were detected by transmission electron microscopy (TEM; Tecnai G^2). The oxidation states of the samples before and after adsorption were determined by X-ray absorption spectroscopy (XAS) under the 3.2 and 5.2 beamlines (SLRI) in the intermediate photon energy ranges of Cr *K*-edge (5.7–6.7 keV), Fe *K*-edge (7.0–8.0 keV), Fe L_3-edge (0.7–0.73 keV) and O *K*-edge (5.2–5.5 keV), respectively. The chemical states of Fe, Cr and O were analyzed by X-ray photoelectron spectroscopy (XPS; PHI5000 Versa Probe II, ULVAC-PHI, Japan) at the SUT-NANOTEC-SLRI Joint Research Facility, 5.2 beamline.

Synthetic procedures

Synthesis of α-FeOOH. Goethite (α-FeOOH) was synthesized by the following hydrothermal route.[32] Iron solution was prepared by dissolving 4.85 g of $Fe(NO_3)_3 \cdot 9H_2O$ into 10 mL of deionized (DI) water. The solution was then slowly dropped into 10 mL of 4.8 M KOH solution. The mixture was transferred to a Teflon-lined autoclave and crystallized at 100 °C for 6 h. The crystallized sample was then washed with DI water and ethanol several times, and the resultant brown powder of goethite was dried overnight at 50 °C.

Synthesis of Fe_3O_4. Magnetite (Fe_3O_4) was synthesized by the following route.[33] 1.94 g of $FeCl_3$ solution was dissolved into 40 mL of EG in a two-necked round-bottom flask under N_2 atmosphere. The solution mixture was stirred for 30 min and then 10 mL of 1.35 M NaOAc in EG was then added. After 3 h, the mixture was transferred to a Teflon-lined autoclave and heated to 190 °C for 24 h. The obtained powder was separated by a magnetic bar. The resultant black powder of Fe_3O_4 was washed with DI water and ethanol several times and dried overnight at 50 °C.

Cr^{6+} adsorption analysis. A stock solution of 100 ppm Cr^{6+} was prepared from $K_2Cr_2O_7$. Working solutions with desired concentrations were prepared by diluting the stock solution with DI water. Adsorption experiments were carried out by adding each adsorbent to 50 mL of Cr^{6+} solution and stirring vigorously. After adsorption, the adsorbents were separated from the solution by centrifugation for α-FeOOH and using a magnet for Fe_3O_4. Cr^{6+} concentrations were determined by the colorimetric method. Each sampling solution was added to 1,5-diphenylcarbazide ligand with 10% (v/v) of H_2SO_4 (pH = 2) to form chromium complex. The absorbance of this complex was collected by using UV-Vis spectrophotometry at λ_{max} = 540 nm.[34,35] The Cr adsorption capacity of the absorbents (mg g^{-1}) was calculated as

$$\text{Adsorption capacity } (q_e) = \frac{(C_0 - C_e)}{W} V,$$

where C_0 (mg L^{-1}) and C_e (mg L^{-1}) are the initial and equilibrium metal concentrations, respectively, V (L) is the solution volume, and W (g) is the adsorbent weight.

Adsorption isotherms were detected by the Langmuir (eqn (1)) Freundlich (eqn (2) and (3)), Dubinin–Radusckevisch–Kanager (eqn (4)–(6)) and Temkin (eqn (7)) models.[36]

$$\frac{C_e}{q_e} = \frac{1}{bQ_m} + \frac{C_e}{Q_m}, \quad (1)$$

$$q_e = K_f C_e^{1/n}, \quad (2)$$

$$\log q_e = \log K_f + \frac{1}{n} \log C_e, \quad (3)$$

$$\ln q_e = \ln q_{(D-R)}(-\beta\varepsilon^2), \quad (4)$$

$$\varepsilon = RT \ln\left(1 + \frac{1}{C_e}\right), \quad (5)$$

$$E = \frac{1}{\sqrt{2\beta}}, \quad (6)$$

$$q_e = k_1 \ln(k_2) + k_1 \ln C_e, \quad (7)$$

where q_e is the amount of adsorbed Cr^{6+} (mg g^{-1}), C_e is the equilibrium concentration (mg L^{-1}), b is the adsorption equilibrium constant (L mg^{-1}), Q_m (mg g^{-1}) is the maximum

adsorption capacity for the Langmuir model, K_f is Freundlich constants (mg g^{-1} (L mg)$^{-1/n}$) and n is heterogeneity factor, representing the adsorption capacity and the adsorption intensity, respectively. $q_{(D-R)}$ is the theoretical adsorption capacity (mg g^{-1}), β is a constant related to adsorption energy for a mole of the adsorbate (mol^2 kJ^{-2}), R is the ideal gas constant (0.008314 kJ K^{-1} mol^{-1}), T is the absolute temperature (K), E (kJ mol^{-1}) is the mean free energy per molecule of adsorbate when it transfers from the bulk of the solution (infinity) to the adsorbent surface, k_1 and k_2 are Temkin constants, where k_1 is related to the heat of adsorption (J mol^{-1}) and k_2 is the equilibrium binding constant (L g^{-1}).

The adsorption thermodynamics of α-FeOOH and Fe_3O_4 was determined at the temperatures of 25 °C, 40 °C and 60 °C using 1 ppm Cr^{6+} solution and 0.02 g of each adsorbent. The effects of different initial Cr^{6+} concentrations (1–20 ppm), adsorbent doses (0.02–0.1 g), and contact times (10–90 min) in the Cr adsorption efficiency were investigated. The optimization of pH for Cr^{6+} removal was conducted in the range of 1–7, which covers the point of zero charges (PZC) of both absorbents.

The stability and adsorption behavior of Cr species on adsorbent surfaces were investigated by performing a reusability test. Each adsorbent was separated from the solution and dried overnight at 50 °C before starting a new cycle.

Results and discussion

Structures of α-FeOOH and Fe_3O_4

The crystal structures of as-synthesized and Cr-adsorbed Fe_3O_4 and α-FeOOH were determined by XRD as shown in Fig. 1a and b, respectively. The XRD pattern of α-FeOOH indicated its orthorhombic structure. The lattice constants of α-FeOOH structure were calculated as $a = 4.611$ Å, $b = 9.962$ Å, $c = 3.024$ Å (JCPDS no. 29-0713).[37,38] The diffraction pattern of Fe_3O_4 indicated its cubic structure (JCPDS no. 19-0629)[28,39] with a lattice constant of $a = b = c = 8.364$ Å. The phase indexing and the refined unit cell parameters were reported in ESI data S1† and their corresponding XRD refinement in S2–S5.† Specifically, the Fe_3O_4 and Cr@Fe_3O_4 samples were indexed as magnetite Fe_3O_4 phase (cubic, space group $Fd\bar{3}m$), while the α-FeOOH and Cr@FeOOH samples were indexed as iron (III) oxide hydroxide goethite phase (orthorhombic, space group *Pbnm*).

A closer inspection of the refinement results, the addition of chromium species into the materials led to a slight shrinkage of the unit cell parameters compared to the pristine materials. This observation suggested the incorporation of Cr^{3+} into the material matrix of Fe_3O_4 (or FeOOH) without the presence of an additional crystalline impurity phase. In these cases, the atomic site occupancy could not be precisely defined. In addition, XAS was used to propose the local structures of Cr and Fe species in the obtained materials.

The TEM images and lattice parameters of α-FeOOH and Fe_3O_4 are displayed in Fig. 2. The α-FeOOH exhibited short-range-order and rod-like structures (Fig. 2a). The selected area electron diffraction (SAED) pattern of rod-like particles confirmed the orthorhombic structure of α-FeOOH with the (130) and (061) characteristic planes. Its particle size was in the range of 620 (±219) × 55 (±21) nm as shown in S6.† The TEM image of Fe_3O_4 in Fig. 2b revealed spherical particles of 400 ± 124 nm with characteristic planes of (311) and (422).[33] The BET surface areas of α-FeOOH and Fe_3O_4 were 84 m^2 g^{-1} and 32 m^2 g^{-1}, respectively. The larger particle size of Fe_3O_4 led to a lower surface area.

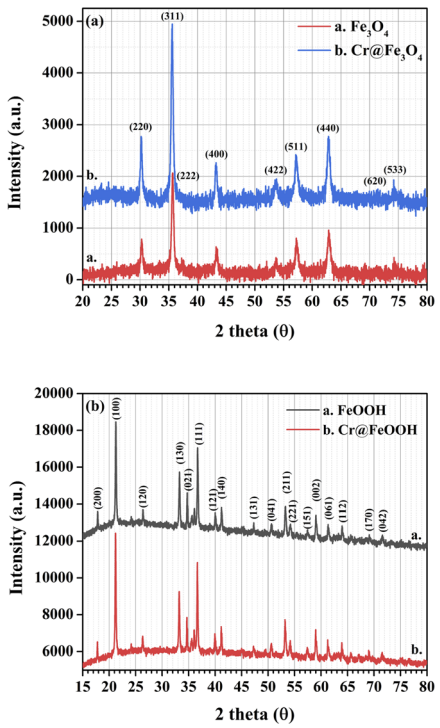

Fig. 1 XRD patterns of as-synthesized and Cr-adsorbed (a) Fe_3O_4 and (b) α-FeOOH.

Cr-adsorption ability

Effect of pH. The PZC values of Fe_3O_4 and α-FeOOH were 5.95 ± 0.04 and 3.95 ± 0.06, respectively (S7†). The Cr-adsorption dependency on pH is shown in Fig. 3. When pH < PZC, surfaces of Fe_3O_4 and α-FeOOH are protonated to a positive charge. Thus, the adsorption behavior of Fe_3O_4 and α-FeOOH is facilitated by an electrostatic mechanism with negative Cr-compounds ($HCrO_4^-$, CrO_4^{2-}, and $Cr_2O_7^{2-}$).[40] The adsorbent surface does not favor Cr^{6+} adsorption with a pH increase.[41] The highest Cr-adsorption ability of both adsorbents was detected at pH = 3.

Fe_3O_4 had a higher Cr-adsorption ability than α-FeOOH, indicating its stronger attraction to the negative compounds of Cr^{6+}. Thus, pH = 3 was selected as the optimized value to reach the maximum capacity of the adsorbents. The maximum Cr^{6+} uptakes by α-FeOOH and Fe_3O_4 were determined as about 2.08 mg g^{-1} and 2.87 mg g^{-1}, respectively. In addition, the effects of adsorbent dose, initial concentration and contact time of Cr-adsorption were discussed in S8–S10.†

Adsorption behavior of Fe_3O_4 and α-FeOOH

Adsorption kinetics. The kinetic parameters of Cr^{6+} adsorption on α-FeOOH and Fe_3O_4 are summarized in S13.† The given

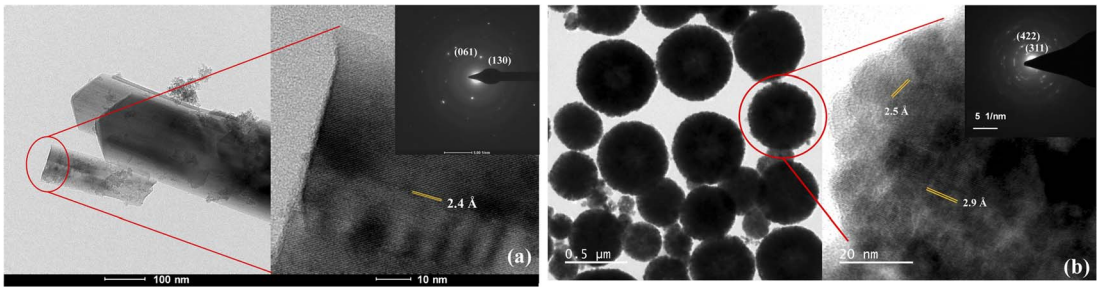

Fig. 2 TEM images of (a) α-FeOOH and (b) Fe_3O_4.

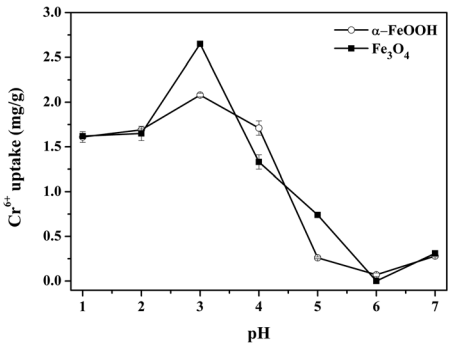

Fig. 3 Effect of pH on Cr^{6+} uptake by the Fe_3O_4 and α-FeOOH adsorption condition: Cr^{6+} initial concentration = 1 ppm, adsorbent dose = 0.4 g L^{-1}, time = 30 min.

correlation coefficient (R^2) of the adsorbents obeyed the pseudo-second order model. The model implies that the rate law for adsorption is described in terms of an initial concentration of Cr rather than in terms of adsorbent concentration. In addition, the chemisorption process is implicated in a rate-determining step of Cr on both ion-oxides.[45,46]

Adsorption thermodynamics. Adsorption isotherms were fitted based on the Langmuir and Freundlich, Dubinin–Radusckevisch–Kanager and Temkin models (S11†), and the corresponding fitting parameters and correlation coefficients are listed in S12.† The Cr^{6+} adsorption behaviors of α-FeOOH and Fe_3O_4 obeyed the Langmuir model (higher regression coefficient (R^2)) indicating that adsorption takes place at a specific homogeneous site, and monolayer coverage was formed on the adsorbent surface.[42–44] A low b value implied a strong binding ability.[28] Therefore, the lower b value of Fe_3O_4 indicated its stronger Cr^{6+} adsorption ability than that of α-FeOOH.

The thermodynamic parameters of α-FeOOH and Fe_3O_4 are listed in S14.† Gibb's free energy changes (ΔG°) for both adsorbents had negative values, confirming a spontaneous nature of adsorption.[34] An α-FeOOH had a negative standard enthalpy change (ΔH°) implying an exothermic process.[47] α-FeOOH had a negative entropy change (ΔS°) indicating the decreased randomness at the solid/solution interface.[48] In contrast, Fe_3O_4 showed an endothermic process from a positive ΔH° value indicating that an ion-exchange on the adsorbent surface might occur.[49] The positive ΔS° of Fe_3O_4 implied randomness at the solid–solution interface during the adsorption process due to adsorption and subsequent desorption.[48]

The reusability of both adsorbents for five cycles is shown in Fig. 4 to support the thermodynamic hypothesis of α-FeOOH and Fe_3O_4. Different adsorption behaviors of the adsorbents were exhibited. The Cr^{6+} uptake of Fe_3O_4 dramatically decreased (90–95%) in the subsequent cycles. On the other hand, the Cr^{6+} uptake of α-FeOOH slowly decreased by 55–60% in the subsequent cycles. These results implied that the Fe_3O_4 surface was completely adsorbed by Cr-species and it was difficult to detach from the surface. In contrast, the α-FeOOH surface was weakly adsorbed by the adsorbent due to a weak interaction (physisorption) which probably detached from the surface.

Analysis of the adsorbed species on adsorbents

Surface analysis of α-FeOOH and Fe_3O_4 by XPS. The oxidation states of surface elements in the pristine and Cr-adsorbed adsorbents were analyzed by XPS (Fig. 5). The C 1s peak at 284.8 eV was used as a reference to correct electrostatic charging. The binding energies of Fe $2p_{3/2}$ and Fe $2p_{1/2}$ in Fig. 5a and b corresponded to Fe_3O_4 and α-FeOOH. The peaks of octahedral Fe^{2+}, octahedral Fe^{3+}, and tetrahedral Fe^{3+} at 710.7 eV, 711.7 eV, and 714.1 eV were determined in the pristine Fe_3O_4 sample corresponded to the typical Fe_3O_4 structure. The corresponding energies of Cr@Fe_3O_4 were found at 710.3 eV, 711.7 eV, and 713.9 eV, respectively, which were slightly lower

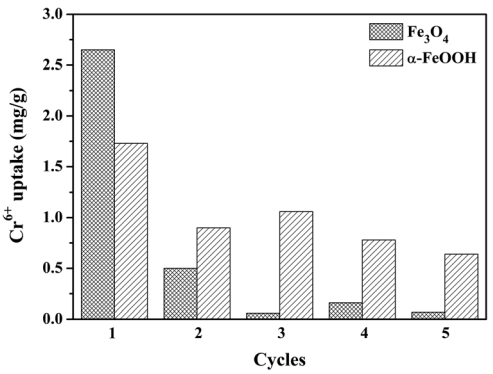

Fig. 4 Reusability for Cr^{6+} removal of Fe_3O_4 and α-FeOOH adsorbents with Cr^{6+} initial concentration = 1 ppm, adsorbent dose = 0.4 g L^{-1}, pH = 3, time = 30 min.

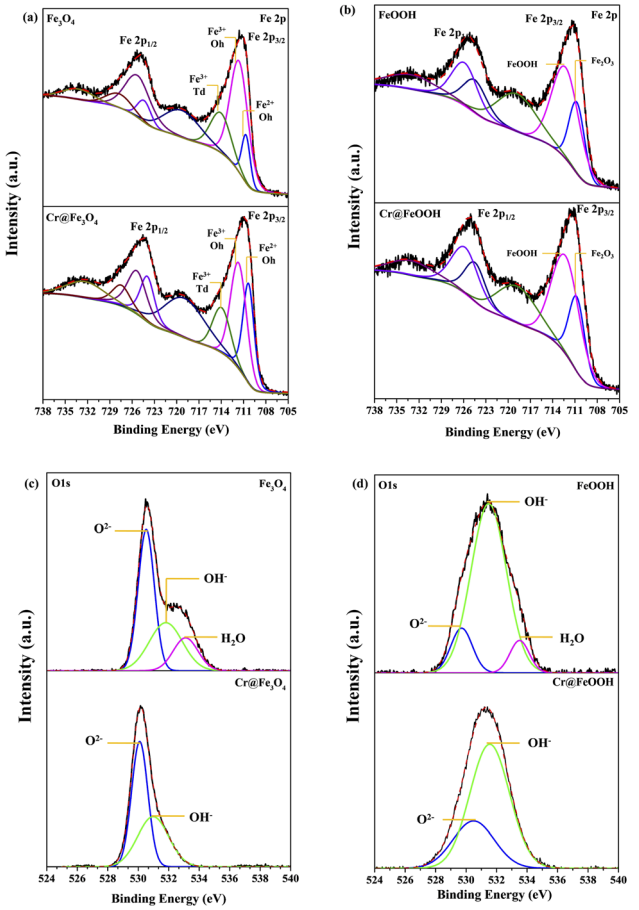

Fig. 5 Fe 2p XPS spectra before and after Cr^{6+} adsorption of (a) Fe_3O_4 and (b) α-FeOOH and O 1s spectra before and after Cr^{6+} adsorption of (c) Fe_3O_4 and (d) α-FeOOH.

than those of the pristine Fe_3O_4. In addition, the area ratio of $Fe^{2+}{}_{Oh}/Fe^{3+}{}_{Oh}$ in Cr@Fe_3O_4 was higher than the pristine Fe_3O_4. The result indicated a decrease of $Fe^{3+}{}_{Oh}$ in Fe_3O_4 after Cr-adsorption. The Fe 2p energies at 710.7 eV and 712.3 eV corresponding to Fe_2O_3 and α-FeOOH components, respectively, were observed on both the pristine α-FeOOH and Cr@FeOOH.[50] It was implied that surface species of α-FeOOH were not changed after Cr-adsorption.

The O 1s peaks of pristine Fe_3O_4 at 530.5 eV, 531.8 eV, and 533.1 eV appeared from lattice oxygen ($O^{2-}{}_{lattice}$), oxygen in the adsorbed-hydroxyl group (OH_{ads}), and oxygen in water-adsorbed molecules (H_2O_{ads}), respectively (Fig. 5c and d). After Cr adsorption, the binding energies of $O^{2-}{}_{lattice}$ and OH_{ads} slightly decreased to 530.1 eV and 530.9 eV, respectively, indicating a presence of $O^{2-}{}_{lattice}$ in CrO(OH) over the Fe_3O_4 surface.[51–53] The results exhibited a partial ion-exchange Cr^{3+} in Fe^{3+} sites which well corresponded to the decrease of $Fe^{3+}{}_{Oh}$ constituent as mentioned in the Fe 2p energy. Moreover, no peak corresponding to water-adsorbed species on Cr@Fe_3O_4 was determined because Cr-adsorbed species fully covered the Fe_3O_4 surface. The O 1s peaks of α-FeOOH at 530.5, 530.5 and 531.5 eV corresponded to $O^{2-}{}_{lattice}$, OH_{ads} and adsorbed H_2O species, respectively. The adsorbed H_2O was not determined on Cr@FeOOH. In addition, the binding energy of $O^{2-}{}_{lattice}$ in Cr@FeOOH was slightly higher than that in α-FeOOH. These results possibly indicate the presence of precipitate oxide form of Cr_2O_3 on the α-FeOOH surface.

The binding energies of Cr $2p_{3/2}$ and Cr $2p_{1/2}$ in Cr@Fe_3O_4 and Cr@α-FeOOH are shown in Fig. 6. The Cr $2p_{3/2}$ to Cr $2p_{1/2}$ splitting energies of both samples were about 10 eV which was typically found in a Cr^{3+}/Cr^{6+} mixture.[54] The Cr $2p_{3/2}$ exhibited the characteristics of Cr^{3+} in Cr_2O_3 (576.6 eV), $CrO(OH)/Cr(OH)_3$ (577.7 eV) and Cr^{6+} in CrO_3 (579.9 eV).[7,42,44,50–54] Those characters were similarly found in Cr@Fe_3O_4 and Cr@FeOOH. However, the area ratio of Cr_2O_3/CrO(OH) in Cr@FeOOH was higher than that in Cr@Fe_3O_4. The finding correlated with the enhancement of $O^{2-}{}_{lattice}$ species of Cr@FeOOH in O 1s spectrum. This result revealed the presence of precipitated Cr_2O_3 species on the α-FeOOH surface at pH 3.[55] It was noticeable that a high CrO(OH) content in Cr@Fe_3O_4 might proceed through Cr^{3+} migration on the Fe_3O_4 surface.

Bulk analysis of α-FeOOH and Fe_3O_4 by XAS

XANES of Fe *K*-edge and L_3-edge. The Fe *K*-edge spectra of Fe_3O_4 and α-FeOOH compared with the iron oxide standards are shown in Fig. 7. The Fe *K*-edge energy of the pristine Fe_3O_4 was calculated as 7120.7 eV while the energy of Cr@Fe_3O_4 slightly shifted to a lower value of 7120.5 eV. This result indicated that ferrous specie (Fe^{2+}) in Fe_3O_4 increased after Cr-adsorption. On the other hand, the Fe *K*-edge energies of the pristine α-FeOOH and Cr@FeOOH were similar (Fig. 7b). Thus, the bulk structure of α-FeOOH was not affected by Cr-adsorption process.

In principle, Fe L_3-edge has a better resolution for fine structures and manifests a lower intrinsic lifetime broadening than Fe *K*-edge. Thus, the local geometry of Fe_3O_4 was further investigated by Fe L_3-edge. The spectra of Fe_3O_4 and Cr@Fe_3O_4 are presented in Fig. 7c. The I_a/I_b intensity ratio in the Fe L_3-edge spectrum was used to determine the mixed valence state.[56] The Cr@Fe_3O_4 had I_a/I_b ratio of 0.59 which was higher than that of pristine Fe_3O_4 (0.53). The higher I_a/I_b intensity ratio

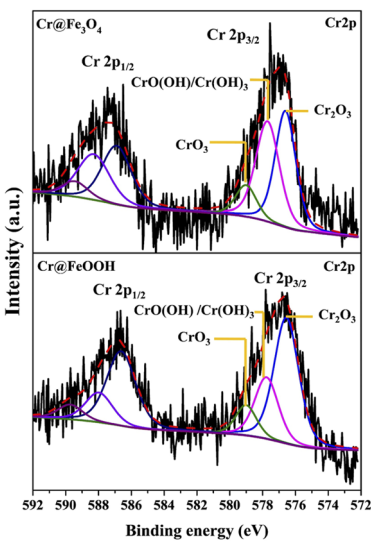

Fig. 6 Cr 2p XPS spectra of Cr@Fe_3O_4 and Cr@FeOOH.

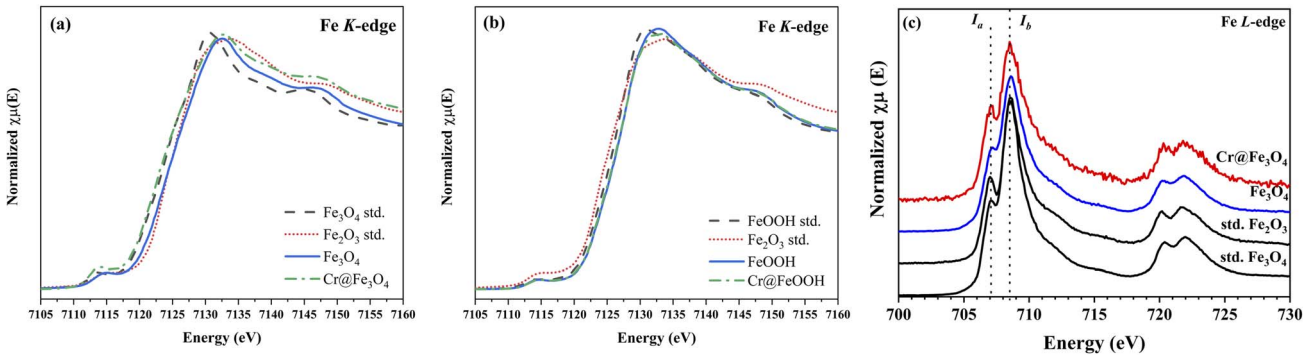

Fig. 7 Fe *K*-edge XANES spectra of bare and Cr-adsorbed (a) Fe_3O_4 and (b) α-FeOOH and (c) Fe L_3-edge XANES spectra of $Cr@Fe_3O_4$ and Cr@FeOOH comparing with the iron standards.

corresponded to the lower Fe^{2+} content in the tetrahedral site of Fe_3O_4.[56]

XANES of Cr *K*-edge. A comparison of Cr *K*-edge in the Cr-adsorbed samples with $CrCl_3$ (Cr^{3+}) and $K_2Cr_2O_7$ (Cr^{6+}) standards are shown in Fig. 8. The Cr^{6+} (4-fold Cr–O) character was exhibited by a strong pre-edge intensity at 5999 eV.[57] Besides, a weak pre-edge intensity was found in Cr^{3+}(6-fold Cr–O). XANES profile of $Cr@Fe_3O_4$ explored a reduction of pre-edge intensity compared with the Cr^{6+} standard. Thus, the Fe_3O_4 could partially reduce Cr^{6+}-species ($HCrO_4^-$, CrO_4^{2-}, $Cr_2O_7^{2-}$) to Cr^{3+} on the surface under aqueous solution at pH 3. This behavior was also observed on Cr@FeOOH.[58] However, a decrease in pre-edge intensity of Cr@FeOOH was much lower than that of $Cr@Fe_3O_4$. Furthermore, Cr^{6+} was a major species in the solution after adsorption (S15†).

XANES of O *K*-edge. The O *K*-edge XANES spectra and their derivative plots of the pristine and Cr-adsorbed Fe_3O_4 and α-FeOOH structures are exhibited in Fig. 9. The O *K*-edge energy of $Cr@Fe_3O_4$ (Fig. 9a) shifted to higher values compared to pristine Fe_3O_4. The result revealed a decrease in the electron density of oxygen atoms in the bulk structure of $Cr@Fe_3O_4$. This finding was probably due to an enhancement of oxygen bonding with a higher ionic strength species of Fe^{3+} rather than Fe^{2+}. Hence, an increase of Fe^{3+}–O component in the $Cr@Fe_3O_4$ structure was suggested. An increase of Fe^{3+} species in $Cr@Fe_3O_4$ was in good agreement with Fe *K*-edge XANES. In addition, on Fig. 9b, O *K*-edge energy of $Cr@Fe_3O_4$ nearly fitted to α-FeOOH. Thus, a part of FeO(OH) as well as CrO(OH) could be created on the Fe_3O_4 structure after Cr-adsorption. Meanwhile, the O *K*-edge energies of α-FeOOH and Cr@FeOOH were similar indicating no structural change in the bulk structure of α-FeOOH during Cr adsorption.

EXAFS analysis of Fe and Cr *K*-edge

EXAFS of Fe *K*-edge. The local structures of Fe_3O_4 and $Cr@Fe_3O_4$ were investigated by Fe *K*-edge EXAFS analysis. The EXAFS analysis is reported in Table 1 and S16.† The 4-fold and 2-fold Fe–O bonds with distances of 1.61 Å and 1.89 Å, respectively, were observed in bare Fe_3O_4. The bond length of 1.61 Å was shorter than the typical tetrahedral Fe–O bond length in Fe_3O_4 (1.88 Å) due to the existence of oxygen vacancies.[59] The second shell of the Fe_3O_4 structure consisted of Fe–O (3.14 Å) and Fe–Fe (3.47 Å) bonds. After Cr adsorption, the first shell represented 2-fold (1.97 Å) and 4-fold (2.40 Å) of Fe–O bonds. The bond distances fitted well with octahedral Fe–O in Fe_2O_3 or tetrahedral Fe–O in α-FeOOH. For α-FeOOH, the first shell consisted of tetrahedral Fe–O bonds with an average bond distance of 1.97 Å (Table 1). Moreover, 3-fold Fe–Fe bonds with bond distances of 3.00 Å and 3.30 Å were also displayed. Octahedral Fe–O (1.98 Å) and Fe–Fe (3.00 Å) bonds in Cr@FeOOH were similar to α-FeOOH. Thus, the bulk structure of α-FeOOH did not change after Cr adsorption.

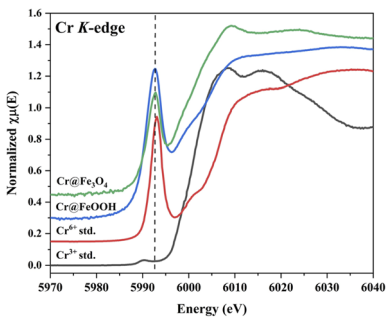

Fig. 8 Cr *K*-edge XANES spectra of $Cr@Fe_3O_4$ and Cr@FeOOH comparing with Cr-standards.

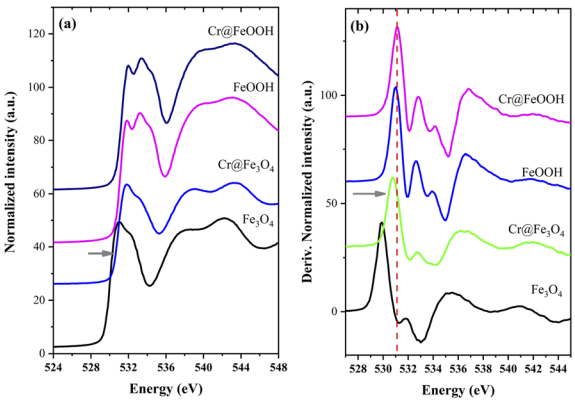

Fig. 9 O *K*-edge XANES spectra (a) and their derivatives (b) of bare and Cr-adsorbed Fe_3O_4 and α-FeOOH.

Table 1 k^2 (χ) weight of Fe *K*-edge EXAFS of bare and Cr-adsorbed Fe_3O_4 and α-FeOOH

Sample	Bond	Distance (Å)	Coordination number (CN)	Debye–Waller factor (σ^2)
Fe_3O_4	Fe–O	1.61	3.9	0.054
	Fe–O	1.89	2.8	0.006
	Fe–O	3.14	12.0	0.048
	Fe–Fe	3.47	12.0	0.013
$Cr@Fe_3O_4$	Fe–O	1.97	2.2	0.012
	Fe–O	2.40	3.8	0.059
	Fe–Fe	2.76	0.9	0.004
	Fe–Fe	3.00	2.9	0.008
	Fe–Fe	3.49	3.2	0.013
α-FeOOH	Fe–O	1.97	4.3	0.012
	Fe–Fe	3.00	3.1	0.012
	Fe–Fe	3.30	3.0	0.013
	Fe–O	3.40	3.0	0.002
	Fe–Fe	3.89	12.0	0.035
Cr@FeOOH	Fe–O	1.98	6.0	0.013
	Fe–Fe	3.00	6.0	0.017
	Fe–O	3.32	6.0	0.003
	Fe–O	3.81	12.0	0.004

EXAFS of Cr *K*-edge. The Cr *K*-edge EXAFS spectrum of $Cr@Fe_3O_4$ is displayed in Fig. 10a. Cr–O bonds consisted of short Cr^{6+}–O bonds (1.22 Å and 1.56 Å) and long Cr^{3+}–O bonds (1.87 Å) (Table S17†).[29] Hence, mixed phases of Cr_2O_3/CrOOH (Cr^{3+}) and CrO_3 (Cr^{6+}) were formed on $Cr@Fe_3O_4$. Moreover, 2-fold Cr–Cr bonds of 2.41 Å and 3.62 Å correlated to binuclear $Cr_2O_7^{2-}$ species which could be physisorbed on the adsorbent in an aqueous solution at pH 3.

The Cr *K*-edge EXAFS analysis of Cr@FeOOH are presented in Fig. 10b and Table S17.† Tetrahedral Cr–O bonds with the bond distances of 1.33 Å and 1.59 Å corresponded to Cr^{6+} in $HCrO_4^-$. Moreover, the average bond distance of 2-fold Cr–Cr bonds of 3.17 Å was found in Cr@FeOOH which was different from Cr–Cr bonds in $Cr@Fe_3O_4$ confirming that the $HCrO_4^-$ species was presented on α-FeOOH.

Removal mechanism of Cr^{6+} on Fe_3O_4 and α-FeOOH. In the solution pH 2.0–6.5, Cr^{6+} in an aqueous solution existed as a predominant form of $HCrO_4^-$ (eqn (8)). This species moved and adsorbed on the surface of both adsorbents. Some Cr^{6+} was reduced to Cr^{3+} or precipitated on surfaces which confirmed by the existence of Cr_2O_3, $CrO(OH)/Cr(OH)_3$ and CrO_3 from XPS surface analysis. Compared with α-FeOOH, the lower Cr_2O_3/CrO(OH) ratio in $Cr@Fe_3O_4$ implied the Cr-ion migration into the bulk structure of Fe_3O_4. XANES and EXAFS as bulk analysis further revealed this behavior. The contained Fe^{2+} species inside Fe_3O_4 could reduce Cr^{6+} in $HCrO_4^-$ to Cr^{3+} (eqn (9)) with a relatively slow reaction rate due to the limited electron transfer rate in the maghemite (Fe_2O_3) passivation layer.[30] Then, Cr^{3+} species migrated to bulk Fe_3O_4 and formed $Fe_{(1-x)}Cr_xOOH$ containing Fe^{3+} and Cr^{3+} in between FeO lattice (eqn (10)). These dissolved octahedral Cr^{3+}–O sites could prevent the bulk structure of Fe_3O_4 from collapsing.[60,61]

$$H_2CrO_4 \rightarrow HCrO_4^- + H^+ \quad (8)$$

$$2HCrO_4^- + 2Fe^{2+} + 10H^+ \rightarrow 2Fe^{3+} + 2Cr^{3+} + 6H_2O + O_2 \quad (9)$$

$$(1-x)Fe^{3+} + (x)Cr^{3+} + 2H_2O \rightarrow Fe_{(1-x)}Cr_xOOH(s) + 3H^+ \quad (10)$$

Additionally, the XPS and XAS results revealed the increase of FeO species in Fe_3O_4 after Cr-adsorption. Thus, the most likely form was a $Fe_{(3-x)}Cr_xO_4$ solid solution containing Fe^{2+} and Cr^{3+} in forms of FeO and Cr_2O_3.[62] The presented species might be created through Cr^{6+} reduction mechanism by FeO in Fe_3O_4 (or $FeO\cdot Fe_2O_3$) structure as expressed by eqn (11).

$$2FeO + 4HCrO_4^- + 4H^+ \rightarrow 2Fe_{(3-x)}Cr_xO_4 + 4H_2O + 3O_2 \quad (11)$$

Meanwhile, α-FeOOH surface changed to positive $[FeO–OH_2]^{2+}$ species at pH = 3.0 (eqn (12)). These $[FeO–OH_2]^{2+}$ molecules could react with the presented negative $HCrO_4^-$ species by an electrostatic force (physisorption) and created $FeO–HCrO_4$ species (eqn (13)).[7] This adsorption behavior did not change the local geometry and oxidation state of iron atoms in α-FeOOH.

$$FeOOH + H^+ \rightarrow FeO–OH_2^+ \quad (12)$$

$$FeO–OH_2^+ + HCrO_4^- \rightarrow FeO–HCrO_4 + H_2O \quad (13)$$

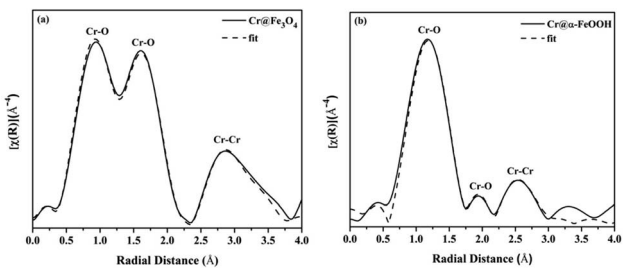

Fig. 10 Fourier transforms of the k^3 (χ) weighted in Cr *K*-edge EXAFS data collected from (a) $Cr@Fe_3O_4$ and (b) Cr@FeOOH.

Conclusions

Fe_3O_4 (magnetite) and α-FeOOH (goethite) synthesized by the hydrothermal method were mainly in cubic and orthorhombic structures, respectively. The Cr adsorption isotherms of Fe_3O_4 and α-FeOOH fitted well with the Langmuir model, indicating a monolayer adsorption process. The maximum Cr^{6+} uptake of 2.87 mg g^{-1} was found by Fe_3O_4. After Cr-adsorption, the Cr^{3+}-doped forms of $Fe_{(1-x)}Cr_xOOH$ and $Fe_{(3-x)}Cr_xO_4$ solid solution was observed in bulk Fe_3O_4 resulting in a high Cr-adsorption capacity. Besides, an electrostatic attraction of $FeO–HCrO_4$ occurred only on the α-FeOOH surface leading to a low Cr-adsorption capacity. The Cr-adsorption ability and behavior in an aqueous solution of the adsorbents were strongly influenced by an adsorbed species stabilized on their structures. The discovered Cr-solid solution in Fe_3O_4 could be a promising catalyst preparation through water treatment process.

Author contributions

Nichapha Senamart-data curation, formal analysis, writing-original draft, writing-review & editing; Krittanun Deekamwong-writing-review & editing; Jatuporn Wittayakun-supervision & editing; Sanchai Prayoonpokarach-review & editing; Narong Chanlek-data analysis; Yingyot Poo-arporn-review & editing; Suttipong Wannapaiboon-data curation, formal analysis, writing; Pinit Kidkhunthod-data analysis and Sirinuch Loiha-conceptualization, funding acquisition, supervision, writing-review & editing.

Conflicts of interest

There are no conflicts to declare.

Acknowledgements

This work was supported by the Science Achievement Scholarship of Thailand (SAST), Center for Innovation in Chemistry (PERCH-CIC). Materials Chemistry Research Center (MCRC), Thailand. Department of Chemistry, Faculty of Science, Khon Kaen University, Khon Kaen, Thailand. Research and Graduate Studies Department, KKU (Research Program, grant number RP64-6/001), fiscal year 2021. Synchrotron Light Research Institute (SLRI), Nakhon Ratchasima, Thailand (BL1.1W, BL2.2, BL3.2Ua, BL5.2 and BL5.3). Suranaree University of Technology (SUT), Thailand Science Research and Innovation (TSRI), and National Science, Research and Innovation Fund (NSRF) (90464/project code 90464).

References

1 A. Chiu, X. L. Shi, W. K. P. Lee, R. Hill, T. P. Wakeman, A. Katz, B. Xu, N. S. Dalal, J. D. Robertson, C. Chen, N. Chiu and L. Donehower, *J. Environ. Sci. Health, Part C: Environ. Carcinog. Ecotoxicol. Rev.*, 2010, **28**, 188–230.
2 M. Narayani and K. V. Shetty, *Crit. Rev. Environ. Sci. Technol.*, 2012, **43**, 955–1009.
3 R. Rakhunde, L. Deshpande and H. D. Juneja, *Crit. Rev. Environ. Sci. Technol.*, 2011, **42**, 776–810.
4 E. J. Tomaszewski, S. Lee, J. Rudolph, H. Xu and M. Ginder-Vogel, *Chem. Geol.*, 2017, **464**, 101–109.
5 L. Li, Y. Li, L. Cao and C. Yang, *Carbohydr. Polym.*, 2015, **125**, 206–213.
6 P. Lazo, *J. Int. Environ. Appl. Sci.*, 2009, **4**, 207–213.
7 S. Wu, J. Lu, Z. Ding, N. Li, F. Fu and B. Tang, *RSC Adv.*, 2016, **6**, 82118–82130.
8 S. R. Chowdhury, E. K. Yanful and A. R. Pratt, *J. Hazard. Mater.*, 2012, **235–236**, 246–256.
9 X. Lv, J. Xu, G. Jiang, J. Tang and X. Xu, *J. Colloid Interface Sci.*, 2012, **369**, 460–469.
10 Y. L. Wei, Y. C. Lee and H. F. Hsieh, *Chemosphere*, 2005, **61**, 1051–1060.
11 A. H. Meena and Y. Arai, *Geochem. Trans.*, 2016, **17**, 1.
12 M. Gheju and I. Balcu, *J. Hazard. Mater.*, 2011, **196**, 131–138.
13 A. Maleki, B. Hayati, M. Naghizadeh and S. W. Joo, *J. Ind. Eng. Chem.*, 2015, **28**, 211–216.
14 M. Gheju, *Water, Air, Soil Pollut.*, 2011, **222**, 103–148.
15 S. M. El-Sheikh, A. B. Azzam, R. A. Geioushy, F. M. El Dars and B. A. Salah, *J. Alloys Compd.*, 2021, **857**, 157513.
16 R. A. Geioushy, S. M. El-Sheikh, A. B. Azzam, B. A. Salah and F. M. El-Dars, *J. Hazard. Mater.*, 2020, **381**, 120955.
17 F. Di Natale, A. Erto, A. Lancia and D. Musmarra, *J. Hazard. Mater.*, 2015, **281**, 47–55.
18 S. M. Lee, L. Lalchhingpuii and D. Tiwari, *Chem. Eng. J.*, 2016, **296**, 35–44.
19 Q. Liu, Q. Liu, W. Ma, W. Liu, X. Cai and J. Yao, *Colloids Surf., A*, 2016, **511**, 8–16.
20 E. I. Basaldella, P. G. Vázquez, F. Iucolano and D. Caputo, *J. Colloid Interface Sci.*, 2007, **313**, 574–578.
21 L. N. Døssing, K. Dideriksen, S. L. S. Stipp and R. Frei, *Chem. Geol.*, 2011, **285**, 157–166.
22 D. L. Sedlak and P. G. Chan, *Geochim. Cosmochim. Acta*, 1997, **61**, 2185–2192.
23 A. E. Gleason, R. Jeanloz and M. Kunz, *Am. Mineral.*, 2008, **93**, 1882–1885.
24 H. Abdel-Samad and P. R. Watson, *Appl. Surf. Sci.*, 1997, **108**, 371–377.
25 T. Mineno and M. Okazaki, *Soil Sci. Plant Nutr.*, 2004, **50**, 1043–1046.
26 V. D. Nguyen, J. Kynicky, P. Ambrozova and V. Adam, *Materials*, 2017, **10**, 783.
27 M. Kumari, C. U. Pittman Jr and D. Mohan, *J. Colloid Interface Sci.*, 2014, **442**, 120–132.
28 S. Rajput, C. U. Pittman and D. Mohan, *J. Colloid Interface Sci.*, 2016, **468**, 334–346.
29 A. H. Meena and Y. Arai, *Geochem. Trans.*, 2016, **17**, 1.
30 J. Chang, H. Wang, J. Zhang, Q. Xue and H. Chen, *Colloids Surf., A*, 2021, **611**, 125784.
31 N. Senamart, J. Watcharakitti, K. Atthawilai, K. Phedluen, P. Nasomjai and S. Loiha, *Suranaree J. Sci. Technol.*, 2018, **25**, 445–454.
32 P. Ou, G. Xu, Z. Ren, X. Hou and G. Han, *Mater. Lett.*, 2008, **62**, 914–917.
33 U. Pal, S. Uribe Madrid and F. Sanchez De-jesus, *Adv. Nano. Res.*, 2014, **2**, 187–198.
34 G. Du, Z. Li, L. Liao, R. Hanson, S. Leick, N. Hoeppner and W. T. Jiang, *J. Hazard. Mater.*, 2012, **221–222**, 118–123.
35 M. Kazemi, M. Jahanshahi and M. Peyravi, *J. Hazard. Mater.*, 2018, **344**, 12–22.
36 O. Ali and S. K. Mohamed, *Turk. J. Chem.*, 2017, **41**, 967–986.
37 F. Geng, Z. Zhao, J. Geng, H. Cong and H.-M. Cheng, *Mater. Lett.*, 2007, **61**, 4794–4796.
38 A. R. Amani-Ghadim, S. Alizadeh, F. Khodam and Z. Rezvani, *J. Mol. Catal. A: Chem.*, 2015, **408**, 60–68.
39 S. Alibeigi and M. R. Vaezi, *Chem. Eng. Technol.*, 2008, **31**, 1591–1596.
40 Y. F. Shen, J. Tang, Z. H. Nie, Y. D. Wang, Y. Ren and L. Zuo, *Sep. Purif. Technol.*, 2009, **68**, 312–319.
41 N. Guo, X. Lv, Q. Li, T. Ren, H. Song and Q. Yang, *Microporous Mesoporous Mater.*, 2020, **299**, 110101.

42 Z. Liu, G. Chen, L. Xu, F. Hu and X. Duan, *ChemistrySelect*, 2019, **4**, 13817–13827.
43 M. Bhaumik, A. Maity, V. V. Srinivasu and M. S. Onyango, *J. Hazard. Mater.*, 2011, **190**, 381–390.
44 S. U. N. Zhenya, Z. H. U. Chunshui, H. Jiangbo, G. Wenqi, C. Hesheng and M. U. Shanbin, *Acta Geol. Sin.*, 2006, **80**, 597–603.
45 X. Q. Zhang, Y. Guo and W.-C. Li, *RSC Adv.*, 2015, **5**, 25896–25903.
46 M. Ahmaruzzaman, *Adv. Colloid Interface Sci.*, 2011, **166**, 36–59.
47 G. Vijayakumar, R. Tamilarasan and M. Dharmendirakumar, *J. Mater. Environ. Sci.*, 2012, **3**, 157–170.
48 M. Hasanpour and M. Hatami, *Adv. Colloid Interface Sci.*, 2020, **284**, 102247.
49 Y. H. Li, Z. Di, J. Ding, D. Wu, Z. Luan and Y. Zhu, *Water Res.*, 2005, **39**, 605–609.
50 A. P. Grosvenor, B. A. Kobe, M. C. Biesinger and N. S. McIntyre, *Surf. Interface Anal.*, 2004, **36**, 1564–1574.
51 X. Zhang, W. G. Sloof, A. Hovestad, E. P. M. van Westing, H. Terryn and J. H. W. de Wit, *Surf. Coat. Technol.*, 2005, **197**, 168–176.
52 Z. Wen, J. Ke, J. Xu, S. Guo, Y. Zhang and R. Chen, *Chem. Eng. J.*, 2018, **343**, 416–426.
53 Z. Wen, Y. Zhang, S. Guo and R. Chen, *J. Colloid Interface Sci.*, 2017, **486**, 211–218.
54 Z. Wen, Y. Zhang, G. Cheng, Y. Wang and R. Chen, *Chemosphere*, 2019, **218**, 1002–1013.
55 S. M. Walker, M. C. Marcano, W. M. Bender and U. Becker, *Chem. Geol.*, 2016, **429**, 60–74.
56 B. P. von der Heyden, A. N. Roychoudhury, T. Tyliszczak and S. C. B. Myneni, *Am. Mineral.*, 2017, **102**, 674–685.
57 S. Ould-Chikh, O. Proux, P. Afanasiev, L. Khrouz, N. Hedhili Mohamed, H. Anjum Dalaver, M. Harb, C. Geantet, J. M. Basset and E. Puzenat, *ChemSusChem*, 2014, **7**, 1361–1371.
58 C. J. Keturakis, M. Zhu, E. K. Gibson, M. Daturi, F. Tao, A. I. Frenkel and I. E. Wachs, *ACS Catal.*, 2016, **6**, 4786–4798.
59 F. Pinakidou, M. Katsikini, K. Simeonidis, E. Kaprara, E. C. Paloura and M. Mitrakas, *Appl. Surf. Sci.*, 2016, **360**, 1080–1086.
60 S.-f. Niu, Y. Liu, X.-h. Xu and Z.-h. Lou, *J. Zhejiang Univ., Sci., B*, 2005, **6**, 1022–1027.
61 T. Kendelewicz, P. Liu, C. S. Doyle and G. E. Brown, *Surf. Sci.*, 2000, **469**, 144–163.
62 X. Wang, N. Chen and L. Zhang, *Environ. Sci.: Nano*, 2019, **6**, 2185–2194.